Accepted refereed manuscript of: Gao Q, Wang S, Peng T, Peng H & Oliver DM (2020) Evaluating the structure characteristics of epikarst at a typical peak cluster depression in Guizhou plateau area using ground penetrating radar attributes. *Geomorphology*, 364, Art. No.: 107015. https://doi.org/10.1016/j.geomorph.2019.107015

Evaluating the structure characteristics of epikarst at a typical peak cluster depression in Guizhou plateau area using ground penetrating radar attributes

Qiangshan Gao [a,b,c], Shijie Wang [a], Tao Peng [a,d*], Haijun Peng [a], David M Oliver [e]

[a] State Key Laboratory of Environment Geochemistry, Institute of Geochemistry, Chinese Academy of Sciences, Guiyang 550081, China

[b] Center for Lunar and Planetary Sciences, Institute of Geochemistry, Chinese Academy of Sciences, Guiyang 550081, China

[c] University of Chinese Academy of Sciences, Beijing 100049, China

[d] Puding Karst Ecosystem Research Station, Chinese Academy of Sciences, Puding 562100, China

[e] Biological & Environmental Sciences, Faculty of Natural Sciences, University of Stirling, FK9 4LA, UK

1. Introduction

The epikarst zone is the upper weathered boundary of a karst system, accommodating high porosity on or near the surface or at the soil-bedrock interface of many karst landscapes (Jones, 2013). The term "epikarst" was first proposed by Mangin (1974) and then was further interpreted as "subcutaneous" (Williams, 1983), which is the karst morphology of rock beneath the soil. Epikarst is therefore recognised to be the "skin" of the karst (Bakalowicz, 2004). In China, research on epikarst and also the state and significance of epikarst structure in modern karstology has advanced significantly, with much progress headed by the research group of Yuan Daoxian (Zhang et al., 2005; Liu et al., 2007; Yuan et al., 2016).

The epikarst ecosystem of karst environments plays a key role in biogeochemical cycling and energy and material storage and transport (Yuan et al., 2016). The karst plateau is in the centre of the southwest China karst, mainly in Guizhou province. The epikarst of this area is well developed with an average thickness of 2 - 5 m because of the sub-tropical climate (Jiang et al., 2001). Likewise, a dual hydrogeological structure and surface and subsurface hydrological system is also well developed. Previous studies have shown that 2000 - 8000 years is required to produce a 1 cm depth of soil in this pure limestone area (Chen, 1997; Feng et al., 2009). The distribution of soil is shallow and scattered, presenting a unique interlocked feature with the carbonate bedrock known as the epikarst zone. The epikarst plays a critical role in local ecosystem services (Lavelle et al., 2006) and studying the structure of epikarst in the karst area is fundamental for understanding the local ecosystem and for underpinning karstology research.

The methods of studying epikarst structure are mainly based on field section surveys with semi-quantitative characterization, and approaches can include dynamic monitoring of hydrological water chemistry (Liang et al., 2003) and modelling (Labat et al., 1999; Jukic´ et al., 2009). The techniques used to quantify the epikarst structure rely on inference, thus accommodating a degree

* Corresponding author
E-mail address: pengtao@vip.gyig.ac.cn (T. Peng), gaoqiangshan@mail.gyig.ac.cn (Q. Gao)

of uncertainty in the research and resulting models if based on unclear structure information.

In recent years, electromagnetic (EM) prospecting techniques have been gradually applied to the survey of karst areas, due to their non-invasive, high resolution capabilities and advantages of field kit portability. Electrical conductivity investigation is used to detect the location of groundwater (McNeill, 1991; Mitrofan et al., 2008). Al-fares et al. (2002) used conventional GPR wiggle images to characterize the structure of caves and karst features in Mediterranean karsts area. Steelman et al (2015) integrated GPR with EM induction methods to identify epikarst below fluvial sediment along the Eramosa River located in Canada, highlighting the benefits of combining these approaches. The integration of GPR and EM induction with traditional survey methods increase not only the confidence levels, but also the number of observations of the karst site characterization (Doolittle and Collins, 1998). Chalikakis et al. (2011) provides an excellent overview of the application of geophysical methods, including GPR, in karst bedrock structures.

The size of karst features is usually small, except for caves. Small epikarst features such as fractures usually can be reflected by the anomalies of the amplitude, phase and wave shape of GPR. Generally, GPR data is used to interpret these anomalies directly after conventional data are processed. The quality of interpretation depends on the level of experience of the user. In addition, seismic attributes can aid interpretation and have been shown, for example, to decrease the dependence on individual subjective judgment in petroleum geophysical exploration (Chopra and Marfurt, 2005). GPR data and seismic data are similar in terms of wave propagation kinematics and reflection responses to subsurface discontinuities (Neal, 2004). Two key differences between GPR and seismic data are the nature and form of transmitted wavelets, and the assumption about the nature of subsurface conditions, which means that some of the more advanced seismic-based processing methods can perform poorly if applied to GPR data (Jol, 2009). From a processing perspective, the recorded data of both is simply a spatially distributed collection of time-domain, voltage signals. Many basic seismic data processing techniques have been applied to GPR data successfully, in turn improving the GPR sections considerably (Fisher et al., 1992; Young et al., 1995).

Attribute techniques can be seen as the last data processing step prior to interpretation. Many seismic attributes can be applied to GPR data. Referring to the theory of seismic attributes (Chen and Sidney, 1997; Chopra and Marfurt, 2005), GPR attributes are used to extract the geometric, kinematics, dynamics and statistical features of electromagnetic waves from radar recorded data for characterizing the structure and property of the target. Young et al. (1997) first applied seismic attribute techniques to 3-D GPR data, using coherence attributes to display a fluvial-deltaic sequence and channel boundary. Currently, GPR attributes mainly contain six kinds of attributes, such as three instantaneous attributes, amplitude attributes, coherence attributes, texture attributes, curvature attributes and polarization (Zhao et al., 2012). GPR attribute technology has already been successfully applied to geological exploration (Franseen et al., 2007), environmental monitoring (Bradford and Deeds, 2006), polar research (Wang et al., 2008) and archaeological surveys (Zhao et al., 2013). As far as we know, GPR attribute technologies have not been widely used in epikarst structure research.

To investigate the structure of epikarst at a peak cluster depression, we chose two types of typical rock-soil mixture epikarst slope profiles and one depression in the Guizhou karst plateau. In this research, we applied average energy attributes and coherence attributes to study the structure of epikarst slope profiles, and applied average amplitude attributes and coherence attributes to interpret the soil-rock interface position of the depression. Coherence attributes can be used to analyse the similarity of wave shape among neighbouring traces, aiming to identify the position of structural discontinuities. Energy and average amplitude attributes are applied to evaluate the amplitude anomalies of a single trace in two different aspects, in turn revealing the variation of media and layers. Our aim was to use these GPR attributes to help interpret the structure of epikarst more easily and accuratley.

2. Overview of research sites

The three test sites were chosen for their representative epikarst slopes and depression areas. They represent shallow and deep fissure soil rock types of epikarst and peak cluster depressions. The two epikarst slope sites (26°13'16.60" N, 105°45'23.27" E and 26°13'15.39" N, 105°45'23.33" E), referred to as No.1 and No.2 epikarst profiles, respectively, are located near the government building of Maguan town at an elevation of about 1305 m. The depression site (26°13'49.80" N, 105°46'21.22" E) is located in Zhongba village of Maguan Town. Fig.1 shows the location of the three GPR detecting sites in the Houzhai catchment of Puding county, Guizhou province. The epikarst and karst landforms are well developed in this region. This area has a subtropical monsoonal humid climate and the average annual rainfall is 1300 mm. May to October is classified as the rainy season, accounting for 83 - 88 % of the total annual rainfall. The annual average temperature and sunshine duration are 14 ℃ and 1165 hours, respectively. In the area of Maguan town, outcrop rock is mainly composed of small amounts of mud shales in the middle part of the Triassic Guanling formation.

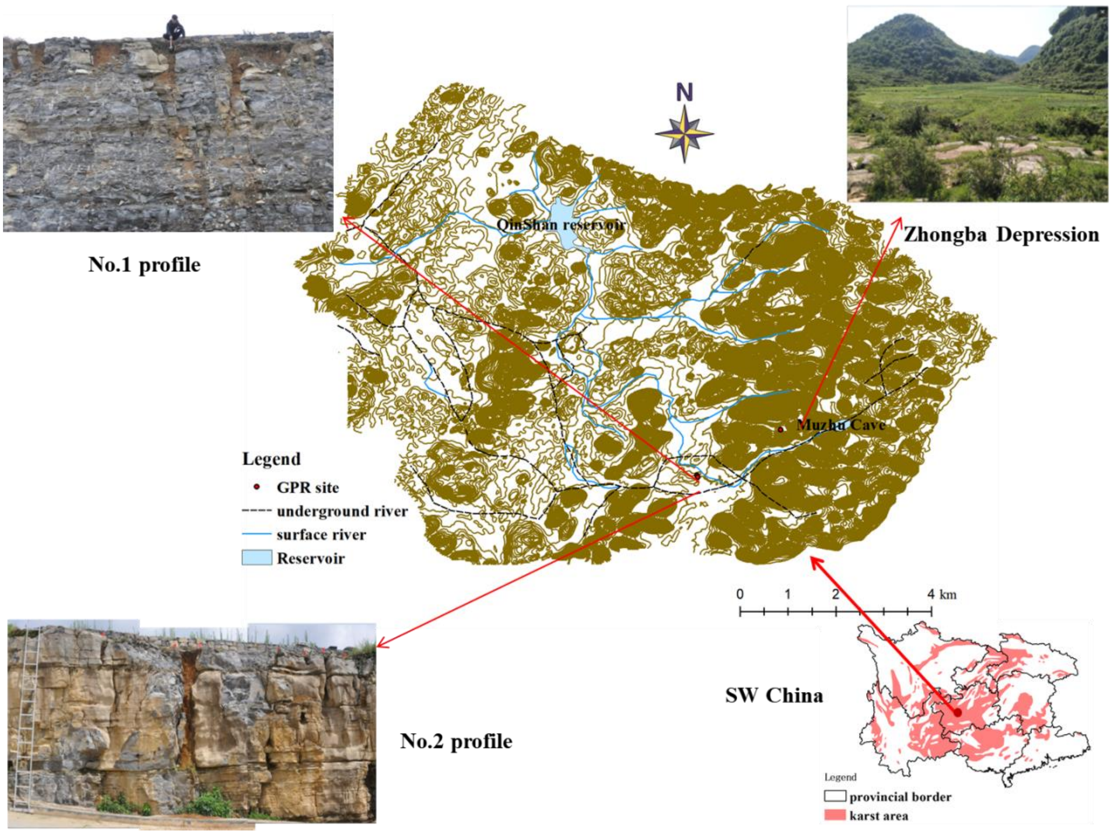

Fig.1 Contour map of the Houzhai catchment in Puding county and the location of GPR detecting sites.

No.1 epikarst profile - shallow fissure soil type

The No.1 epikarst profile accommodates shallow fissure soil development features. Three layers, marked A, B and C by the red dotted lines, are shown in Fig.2. Layer A is the lower boundary of the epikarst. Fissures and grikes above the lower epikarst boundary (A) are common and are filled with soil. Layers B and C are bedding layers filled with sediment, and beneath layer C is mostly rock whereas between layer B and C (~ 4 m depth) there remains some small fissures filled with soil. The exposed rock surface is covered by shallow soil (usually less than 3 cm). The karst development is strong above the layer A, with rock and soil interlocking. The position indicated by the hammer in Fig.2a is the single marker point at this site. The maximum depth of soil-filled fissures is approximately 2 m, with depths of 1 m more common.

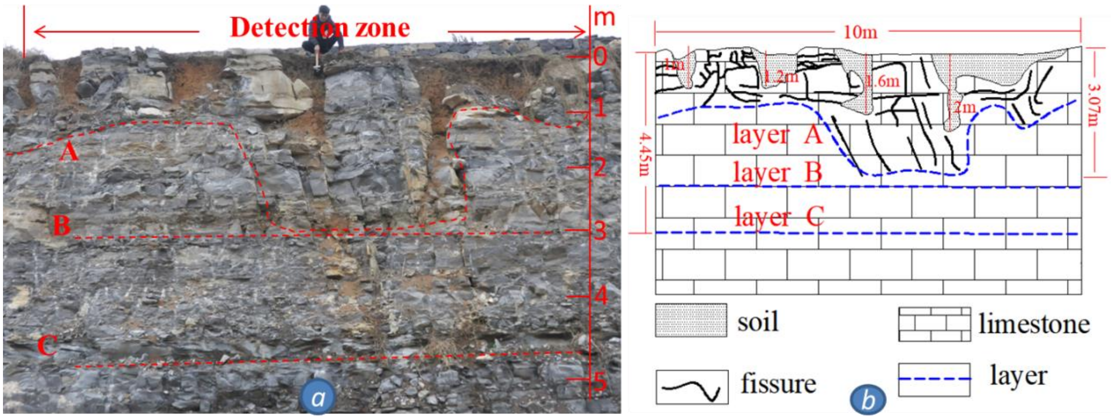

Fig.2 Photograph (a) and sketch map (b) of No.1 epikarst profile

No.2 epikarst profile - deep fissure soil type

The No.2 epikarst profile has three visible bedding layers, referred to as D, E and F from top to bottom (Fig.3). Layer F is the lower boundary of epikarst. Layer G represents the cement or concrete pavement, rather than a geological feature. For scale, the ladder is 30 cm per step. Eight small red flags in the photo identify the extent of detection zone and fissure soil position. The red flag markers (excluding both ends) correspond to the six block markers of the associated GPR images (Fig.11). The deepest soil fissure reaches 3 m depth, with a width of 0.6 m at the surface. The bedrock at both sides of the deepest fissure is exposed, with no soil covering the surface. The bedrock to the right of the deepest fissure has developed more fissures open to the surface. Three fissures are experiencing infilling with soil, with the largest accommodating a width of ~ 15 cm. Two calcite vein bodies are visible, with their position identified on the sketch map (Fig.3b).

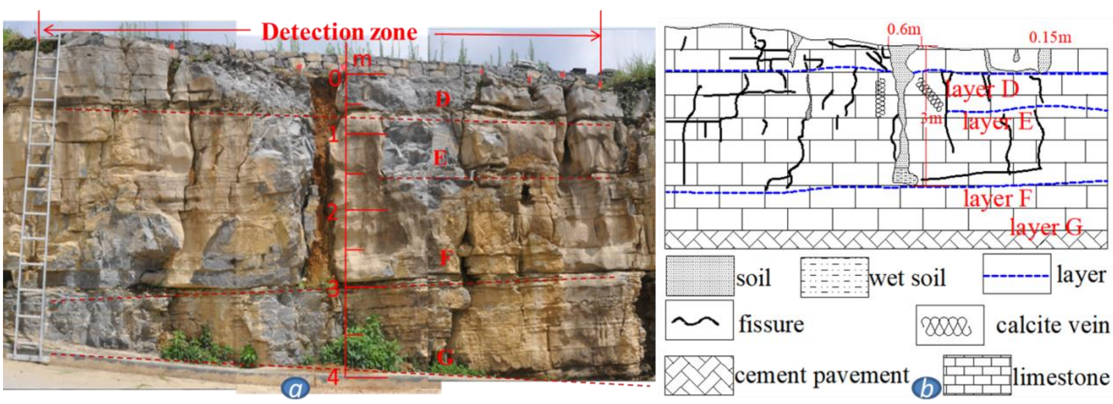

Fig.3 Photograph (a) and sketch map (b) of No.2 epikarst profile

Peak cluster depression - thick soil layer covered type

The depression is surrounded by typical karst hills with the west-facing side providing an entrance point (Fig.4). The depression elevation is 1328 - 1333 m; elevations of the highest and lowest hill are 1520 m and 1440 m, respectively (Yan et al., 2012). Part of the depression is planted with corn and other typical crops, with the remaining area covered with wild grass. In order to avoid crop destruction, the GPR survey line was located in the grassland (Fig.4b). A red flag was positioned every 4 m to enable distance calibration. The soil body mainly comprises wet clay. Prior to the GPR detection, we suspected the soil depth in the depression to exceed 10 m. Thus, the time window of acquisition was set to 1000 ns (see Table 1). Approximately one month later, auger drilling of the soil at the end of the survey line (26°14'2.18"N, 105°46'8.86"E) was undertaken for depth verification (Fig.5).

Fig.4 Photographs of the depression (a) and GPR survey line (b). The red arrow in Fig.4a marks the position of survey line and the red flags in Fig.4b were put every 4 meter on the line. The red inverted triangle in Fig.4a marks the position of auger drilling soil.

Fig.5 Auger soil for depth verification

3. Methods

3.1 Conventional processing procedures

The MALA GPR equipment we used contains the ProEx host and 500 MHz shielded antenna for epikarst evaluation and 50 MHz unshielded Rough Terrain Antenna (RTA) for depression evaluation. Fixed antenna spacings for 500 MHz and 50 MHz were 0.18 m and 4.2 m, respectively. The average detecting depth of 500 MHz is 3 - 5 m and that of 50 MHz is 40 - 70 m. Ground Vision software was used for real-time imaging and monitoring during data acquisition. The acquisition parameters of each site are listed in Table 1. The lateral distance of the epikarst profile was verified by the Master wheel and that of the depression profile was corrected by the markers through REFLEXW software.

Table 1: Acquisition parameters of each site

Site	ANTENNA	Acquisition mode	Sampling Rate	Time window	Trace/time interval	Survey length
No.1 profile	500 MHz shielded	Wheel	7695.4 MHZ	119.3 ns	0.019 m	9.030 m
No.2 profile	500 MHz shielded	Wheel	6215.5 MHz	126.5 ns	0.019 m	9.097 m
Zhongba Depression	50 MHz RTA unshielded	Time	623.9 MHz	1000 ns	0.5 s	40 m

We used REFLEXW 6.0.7 software to undertake conventional processing using the following sequence: 1) the move start time module; 2) the subtract-DC-shift module; 3) the energy decay module; 4) the subtracting average module; 5) the bandpass-butter-worth module; 6) the running average module; 7) f-k filter module; 8) trace interpolation module. Step 7 and 8 were only applied to the data of the depression.

Fig.6 shows the conventional radar image of one demonstration GPR deployment, which was acquired as an exemplar using a site at Puding Karst Ecosystem Research Station (26°21'55.20"N, 105°45'21.48"E). This exemplar enabled us to compare and contrast with the images of its attributes. To facilitate easier observation of the position of strong and weak amplitudes we used both bright and dull colours to display data. Čeru et al. (2018) used this approach to show their GPR data.

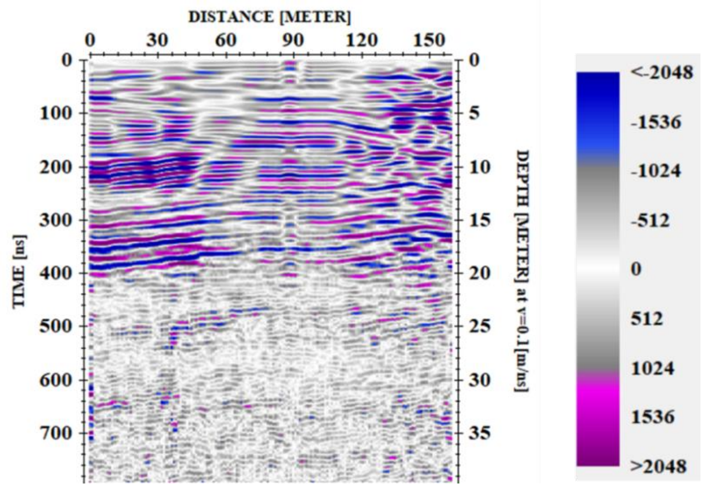

Fig.6 Radar image of exemplar site following conventional data processing, with accompanying colour bar; purple represents strong positive amplitude and blue represents strong negative amplitude; dim grey and white colours represent weak positive and negative amplitude.

3.2 Attribute extracting technology

A large number of attributes have been studied in seismic data interpretation (Chen and Sidney, 1997). Each attribute has the ability to highlight a hidden / difficult-to-visualise feature in the data. Attributes can be analysed without the need for an experienced GPR interpreter. Three attributes were chosen to mine information concerning rock and soil structure of the epikarst and depression sites used in our study, namely: average energy attribute, coherence attribute and average amplitude attribute. We coded the extraction of these three attributes using C Programming Language. The extraction performed better after the conventional processing flows, avoiding noise interference that would otherwise affect the interpretation of attributes.

3.2.1 Energy

The average energy attribute is a common attribute in seismic data interpretation. It is defined as the average value of the sum of the squared amplitude value within a fixed time window in a single trace. The length of the time window is generally set similar to that of the wavelet. Shorter or longer windows would introduce artefacts or decrease the overall resolution (Zhao et al., 2013). All energy values are positive and can magnify the difference of strong and weak amplitudes. Thus, by showing energy variation, the energy attribute can reflect the position of different media. Zhao et al. (2013) extracted energy attributes from 2-D and 3-D GPR data and observed the position of several archaeological features through the variation of energy. For observing the position of soil and rock, this attribute was used to interpret the structure of the No.1 and No. 2 epikarst profiles investigated in this study.

Fig.7 shows the average energy attribute of the demonstration data and can be compared with the conventional radar image (Fig.6), which uses purple and blue to show strong amplitude. In contrast the energy attribute uses only bright purple colouring to show the position of high value (strong amplitude). The strong energy signal of the demonstration data terminates at about 400 ns.

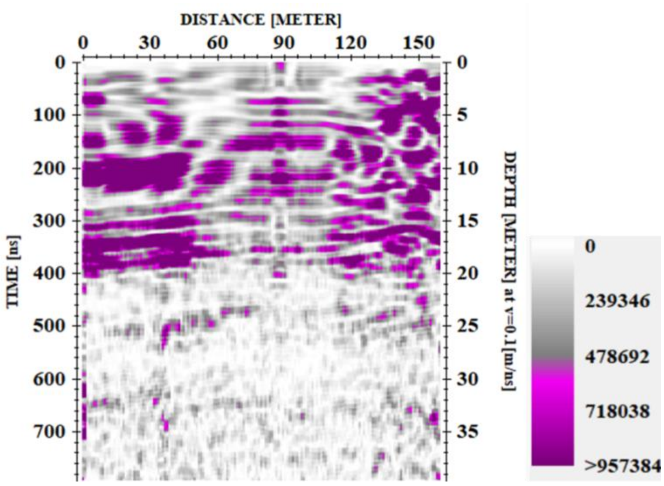

Fig.7 Average energy attribute image of demonstration data and associated colour bar; the bright purple part represents high energy of the signal and the grey and white colour parts reflect low energy.

3.2.2 Average amplitude

The average amplitude attribute is often used to analyse the layers in seismic data interpretation. Its value can be determined by calculating the average of all positive values within a fixed time window, with negative amplitudes discarded. The longer the time window, the greater the reduction in vertical resolution. If the time window contains 3 - 7 samples, the resolution will retain sufficient resolution for our study. This attribute is helpful to interpret the layers' depth.

In contrast to the conventionally processed radar image (Fig.6), interpretation of the layers' depth is easier without the blue colouration, as observed in the figure of average amplitude attribute (Fig.8). We applied such an approach to interpret the soil depth of the depression in this study.

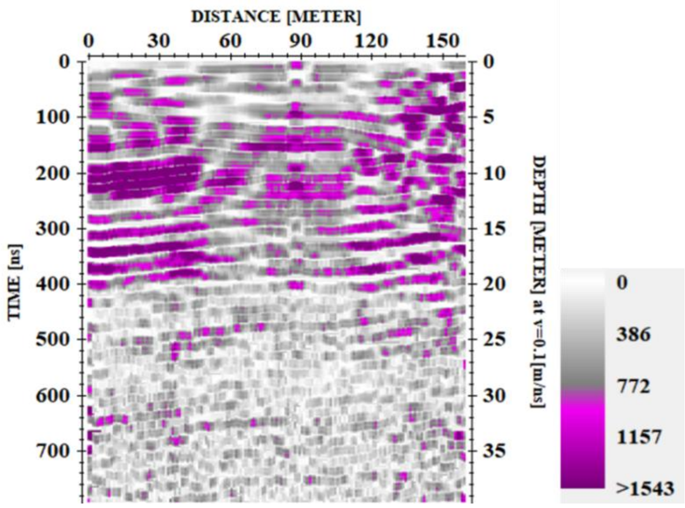

Fig.8 Average amplitude attribute image of demonstration data and associated colour bar; purple represents high amplitude and others are low amplitude values.

3.2.3 Coherence

The coherence attribute was first proposed by Bahorich and Farmer (1995). It was originally applied to interpret the position of discontinuities, such as cracks, faults, etc. Based on the classical mutual correlation algorithm, the coherence attribute quantitatively describes the waveform similarity of multi traces. A value of one is associated with this attribute if traces are identical, and a value of zero is returned if traces have a phase-shift of 180°. The high value represents stronger integrity of the area and thus the presence of fewer developed cracks and faults. Conversely, a low value indicates a higher degree of fractures. Reis et al. (2014) presented the outline of collapsed paleocaves in the host limestone rock by calculating the similarity from 3D GPR data. Its two-dimensional simplified formula by our modification is as follows:

$$\rho_x(x_i, t, Vt_x) = \frac{\sum_{\tau=-\omega}^{\omega} u(x_i, t-\tau)u(x_{i+1}, t-\tau-Vt_x)}{\sqrt{\sum_{\tau=-\omega}^{\omega} u^2(x_i, t-\tau)\sum_{\tau=-\omega}^{\omega} u^2(x_{i+1}, t-\tau-Vt_x)}} \quad (1)$$

Where, u represents radar data, ω is time window and Δt_x denotes time delay.

The coherence attribute image (Fig.9) is much simpler, conveying a two tone output. This output clearly communicates discontinuity in media structure by the black colouration. The coherence attribute is used to interpret all sites investigated in our study.

Note that the black colouration predominates below ~ 400 ns in the demonstration data (Fig.9). Combined with the situation that strong energy terminates at about 400 ns in Fig.7, we consider that the energy of the radar wave decreases to zero at about 400 ns or no more reflection waves are received after 400 ns. The signals after 400 ns are the inherent noise produced by the complete radar system itself, with more detail on such noise reported in Jol (2009). Briefly, the noise here is random, with low energy and low similarity in contrast to the target waves hence black colouration occupies the lower portion of Fig.9 and dim grey occupies the lower portion of Fig.8. No more effective signals or reflected waves are received after 400 ns. Therefore, the use of a coherence attribute can help ensure that the effective area of GPR image is interpreted with greater confidence. In other words, only in the effective area can we use the low coherent value to interpret grikes or fissures.

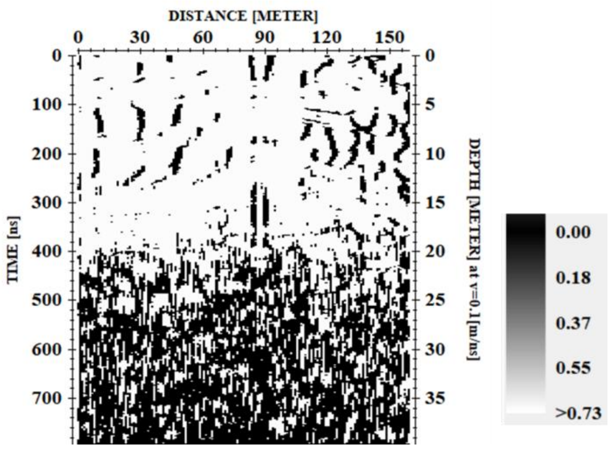

Fig.9 Coherence attribute image of demonstration data and associated colour bar; the white is the high value and the black is the low coherent value.

4 Results

No.1 profile - shallow fissure soil type

Fig.10 shows: (i) the GPR profile after conventional processing; (ii) the average energy attribute;

and (iii) the coherence attribute of the No.1 epikarst profile. All images indicate the position of the marker by a block. The recorded velocity was 0.1 m/ns, representing an average value of rock velocity (>0.1 m/ns) and soil velocity (<0.1 m/ns).

Without the blue colour, the image of the energy attributes looks simpler and approximately represents the distribution of rock and soil of the No.1 profile. Using the marker, it is evident that the fissure soil corresponds to an area of low energy and that conversely the rock corresponds to high energy. Layer C is more pronounced than layer A and B.

Evaluating the coherence attribute (Fig.10c), the area above layer-A (red dotted curve line) is dominated by white colour while the area below A is occupied by black. The effective area is mainly restricted to the zone above layer A according to our analysis of the demonstration data.

High coherent values dominate the effective area, suggesting that the epikarst bedrock has numerous well developed cracks, although the width of most cracks is less than the resolution (about 5 cm) of the 500 MHz GPR. The area dominated by the black colouration likely signals the complete bedrock.

Layer B is more obvious via the coherence attribute (Fig.10c) than via the images presented in Fig.10a and Fig.10b. The reflection signals of layer C, appearing below the effective area, suggest that the predominant black colouration in the area below layer A is due to the lack of an electric impedance reflection interface, and not the radar signal decaying to zero at layer A.

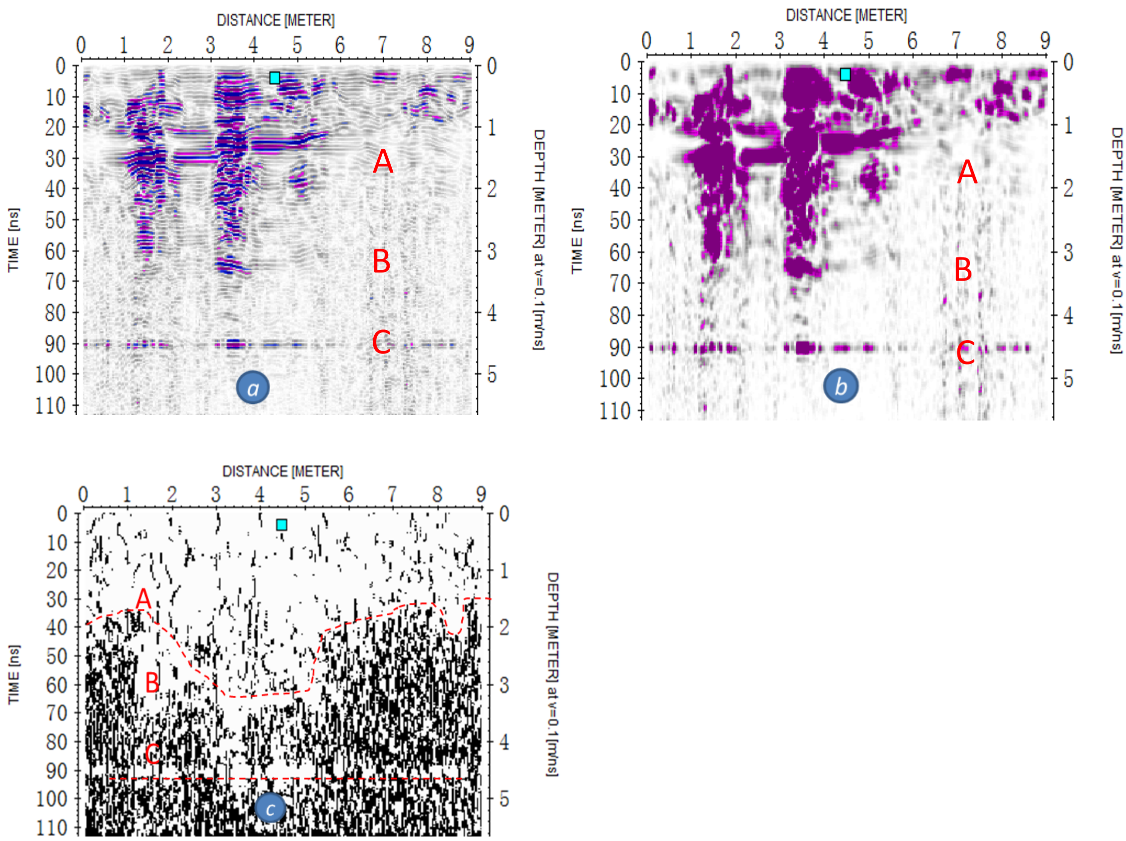

Fig.10 GPR profile images after conventional processing (a), the average energy attribute (b) and the coherence attribute (c) of No.1 epikarst profile. The block markers correspond to the position marked by the hammer in Fig.2. The letters A, B, C and dotted lines indicate the layers' general position.

No.2 profile - deep fissure soil type

Fig.11 shows: (i) the GPR profile after conventional processing; (ii) the average energy attribute; and (iii) the coherence attribute of the No.2 epikarst profile. The recorded velocity was 0.1 m/ns, reflecting the similar media condition of the No.1 profile.

The variation of energy approximately represents the distribution of soil and rock, as inferred through Fig.11b and the markers for the deep fissure soil type. However, the rock below the fissure soil corresponds to a low energy vertical signal. Interpretation of the fissure soil depth using only using the energy attribute is difficult. The width of the observed low energy is not consistent with that of the horizontal range of the soil, likely due to the fixed spacing of the antenna.

Layer G is most recognisable in the energy attribute image (Fig.11c), although layers D, E, and F are all visible and their respective depths reflected by the attribute are approximate to their real depths. Similar to the No.1 epikarst profile, the white area (high coherent value) dominates the area above layer F (epikarst lower boundary), whereas the black colouration is dominant in the area below layer F. The epikarst lower boundary again becomes the threshold of the effective GPR signal area. In addition, the reflected signal of the cement pavement (layer G) appears at 90 ns, which demonstrates that the lack of effective waves below layer F is due to the absence of a radar wave reflection interface rather than the exhaustion of signal.

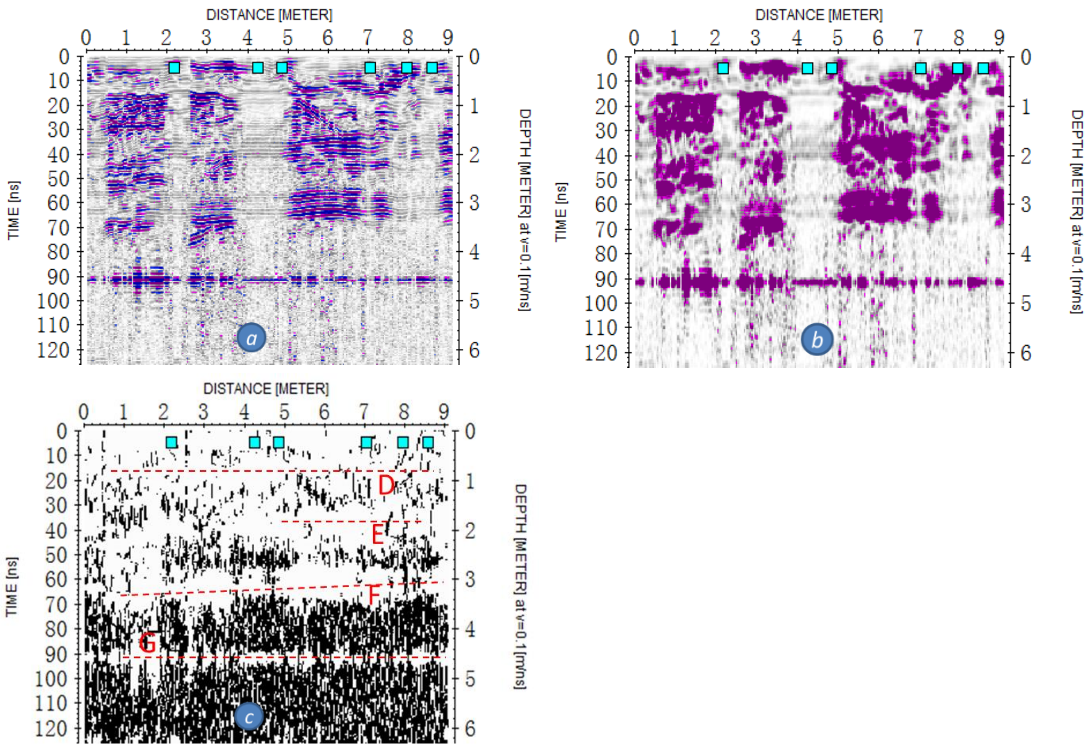

Fig.11 GPR profile images after conventional processing (a), the average energy attribute (b) and the coherence attribute (c) of No.2 epikarst profile. The block markers in the figures are corresponding to small red flags except both ends in Fig.3. The letters D, E, F, G and dotted lines indicate the layers' general position.

Peak cluster depression - thick soil layer covered type

The GPR profile after conventional processing, the average amplitude attribute and the coherence attribute of the depression in the time range of 0-331 ns are shown in Fig.12. The velocity of the electromagnetic wave through wet clay is usually 0.06 m/ns according to Zeng et al. (2010). Table 2 provides information on the soil depth and associated features as determined from the records of our drilling campaign.

Compared with the conventionally processed GPR image (Fig.12a), the average amplitude attribute (Fig.12b) provides a clearer image to interpret the depth of several layers. The deepest interface of strong amplitude is located at 3.6 m depth, as visible in the average amplitude attribute (Fig.12b). If relying solely on conventional radar images to analyse and interpret this environment, those with less interpretation experience are likely to find it difficult to determine which depth is appropriate due to the existence of two pairs of purple and blue horizontal lines at the depth position from 3.2 to 4.2 m in Fig.12a.

The coherence attribute (Fig.12c) shows one continuous white zone at the depth of about 4 m. The area above is dominated by white and the signals have strong amplitude. The area below the 4 m line features a higher degree of black colouration, suggesting that this continuous zone represents the lower boundary of the GPR effective area and the interface of soil and rock. When combined with the result of the average amplitude attribute, we were able to predict the depression soil depth to be ~ 3.6 m, which is very close to the observed depth 3.58 m (see Table 2).

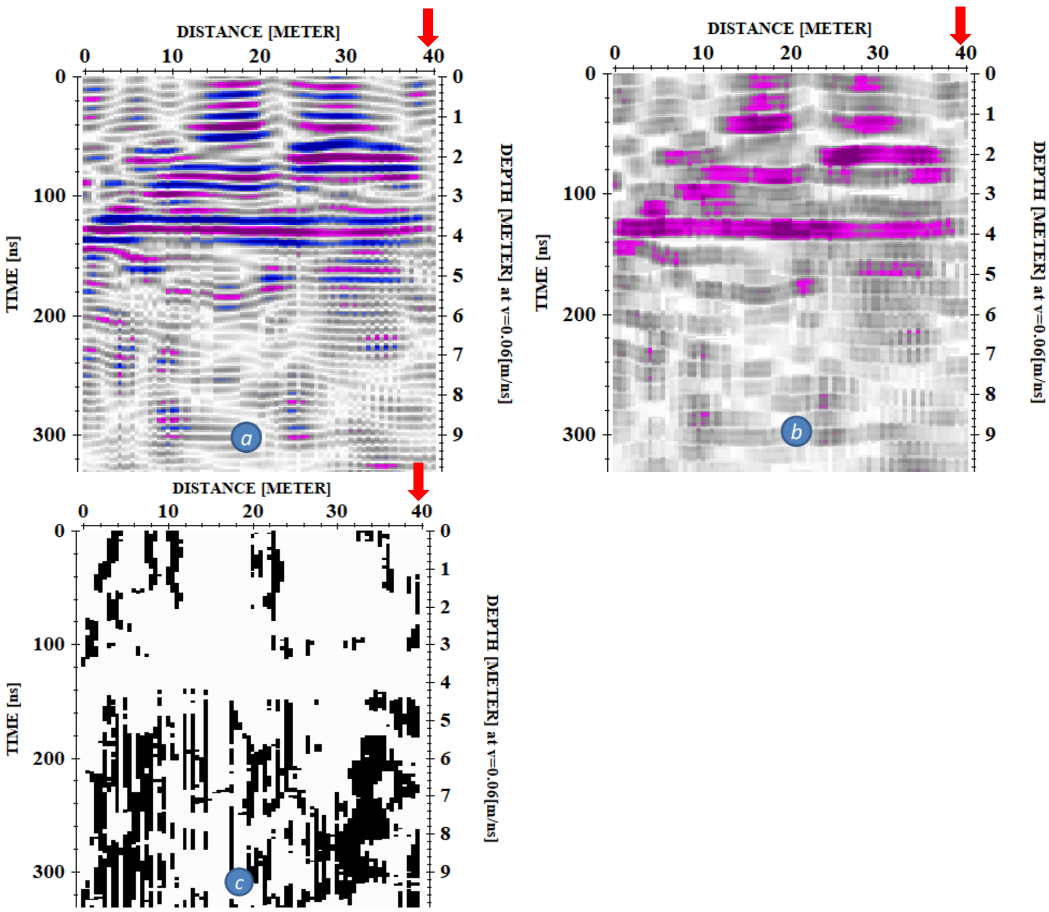

Fig.12 GPR profile after conventional processing (a), the average amplitude attribute (b) and the coherence attribute (c) of the depression data. The red arrows indicate the auger position corresponding to radar images.

Table 2: the soil depth and feature at the verification point

No.	depth	Soil feature	photo

1	60 cm	Soil property change: black colour turn to brown, soil particle become heavier	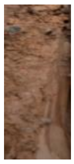
2	100 cm	Soil colour change from brown to dark brown	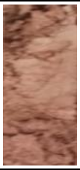
3	140 cm	Particle size become smaller; viscosity become heavier; Humidity increases	
4	163 cm	Reddish brown colour change to greyish yellow. The viscosity remains heavy, but becomes slightly dry	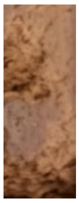
5	187 cm	Carbon pieces appear	
6	214 cm	The colour turns to yellow and shallow; Iron manganese concretion appears	
7	235 cm	Higher viscosity and soil contains little weathered pieces	
8	253 cm	The viscosity become higher and the colour turns dark brown	
9	300 cm	Small rock pieces occur	
10	345 cm	The colour has changed	
11	358 cm	Auger to the interface of limestone bedrock. The sound of rubbing against rock can be heard. Soil sample contains the ground rock pieces	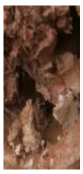

5 Discussion

Results from this study demonstrate that GPR attributes can aid interpretation of the structure of epikarst, particularly the lower interface of the epikarst. Layer A and layer F are the epikarst lower boundaries of shallow and deep fissure soil types, respectively. These two layers split the GPR data into two components with an effective radar signal area located above these lower boundaries of the epikarst layers and non-effective radar areas situated below the lower boundaries. Strong amplitude and high similarity radar signals are more frequent in the effective area relative to the non-effective area. Interpretation of electromagnetic wave propagation is therefore key: the condition of generating the reflection wave is that the electrical properties of the media differ (Zajícová and Chuma, 2019). In the absence of reflected waves, the GPR receiver equipment will acquire inherent random noise signals which have low energy and low coherency relative to an effective refection wave (Jol, 2009; Julayusefi et al., 2012). The rock of the epikarst accommodates many fissures and grikes, which are infilled with soil or sediments, thus easily addressing the condition for reflection waves. In turn, the effective area of the radar image corresponds to the epikarst area. In the non-effective area, layer C of the No.1 profile and layer G of the No.2 profile both deliver a radar signal response. This situation demonstrates that when the electromagnetic wave propagates below the lower layer of the epikarst, the wave does not decay to zero. Given that few signals are reflected back to radar this helps to infer that the electrical properties below the epikarst are almost identical. Therefore, it follows that the epikarst develops with many fissures that are then infilled with soil or other materials, whereas the bedrock below the epikarst maintains its integrity and accommodates similar lithology demonstrated by the GPR energy and coherence attributes.

The GPR attributes are also helpful to interpret the peak cluster depression soil situated in the Guizhou karst plateau. According to the principle of radar waves and the average amplitude and coherence attributes of GPR data, the soil depth we interpreted was close to real depth we measured by auger drilling. A previous study within a small catchment (26°15'36" - 26°15'56" N, 105°43'30" - 105°44'42" E), located relatively close to the Zhongba depression, found that the surface runoff and soil loss of forested land on the karst hill slopes is very low during rainfall events (Peng and Wang, 2012). The vegetation surrounding this depression has not been destroyed abruptly since the Qing dynasty (Yan et al., 2012). Thus, the amount of soil transported by rainfall-runoff processes to the depression each year is likely to be small, with annual soil loss from the slopes to this depression accounting for less than 19.25-27.5 t/km^2 (Yan et al., 2012). This further supports the results we have interpreted from the set of GPR attributes.

The detecting depth of the 50 MHz antenna can exceed 40 m in practice but the depth of an effective signal area in the peak cluster depression was only 3.6 m. We suspect that the bedrock under the depression has a solid structural integrity with few fractures to reflect the radar wave, and future targeted research would help to verify this assumption. Using the boundary of the effective and non-effective areas in the coherence attribute image to interpret the contact of soil and rock is therefore convenient**.** Importantly, while the contact between soil and rock in the average energy attribute output (Fig.11b) appears horizontal this does not imply that the real soil-rock interface is horizontal. If the variation present in the depth of this contact layer does not exceed the resolution (about 15 cm) of the 50 MHz antenna, the GPR image is unlikely to detect this real variation.

The rationale for applying coherence attributes in this study was to attempt to interpret epikarst fractures; however, there were a number of challenges. Though coherence attributes have worked successfully in seismic or other domains, the size and direction of the fractures can complicate readings. For example, the opening size of many fractures at the No.1 and No.2 profiles was less than 3 cm by our measurement. This relatively small size is difficult for a 500 MHz antenna to detect due to the spatial resolution (Alsharahi et al., 2016). In terms of the fractures' direction, we consider that the coherence value varies with the angles or directions of fractures, as suggested by others (Theune et al., 2006). If the direction is horizontal, like the sediment layers, the reflected waves will have high similarity because they are reflected at the same depth, thus the coherence value will be large.

While the results reported here focus on three contrasting sites in Puding county, Guizhou province, the potential for transferability of the approach to other areas of karst terrain is clear. The method reported here can aid in the determination and characterisation of variations in epikarst structure and the findings of our study highlight the usefulness of this approach and its generic application potential in areas far beyond the Chinese karst terrain, which was used here as an exemplar. The approach should therefore be of interest to the wider global scientific community with respect to its application in other areas of the world.

6 Conclusion

GPR attributes and associated mathematical transformations can provide the research community with different views to interpret and characterise epikarst environments, and to make key information more easily accessible. We used three attributes to analyse the structure of epikarst and soil depth of a peak cluster depression in the Guizhou karst plateau karst. Although the resolution decreases, the images of average energy, average amplitude and coherence attributes look simpler and are therefore easier to interpret than the conventional radar image. The energy attribute can reflect the general position of soil and rock in the epikarst horizontally, but it is difficult to confirm all vertical fissure soil depths precisely. Integrating the energy decay and coherence variation of radar signal, the termination position of the effective signal area can be identified, which corresponded with the lower boundary of the epikarst. With respect to the depression, the additional f-k filter process step is crucial for eliminating interference signals reflected by the surrounding mountains before attribute extraction. The depression soil depth was identified by the average amplitude attribute with a low error and helped to minimise interpretation difficulties by the operator.

GPR attributes provide an additional layer of evidence to highlight key epikarst features, such as well-developed fissures infilled with soil or other materials. The approach also serves to demonstrate that the bedrock below epikarst has similar lithology and maintains its structural integrity, identified through energy and similarity information of wave signals. Thus, the study of the general relationship between the slope and depth of epikarst can be improved by using such attributes.

Future research using GPR attributes to inform on epikarst structure should be enhanced through the integration and pursuit of more attributes. Additional research is also required to better understand relationships between coherence values and fracture angles. We used the 500 MHz antenna for the depression survey but this returned little valuable information. Therefore, choosing the appropriate frequency antenna for the context of the research site is undoubtedly important. The resolution of GPR attributes is limited by that of the original data and so the acquisition of high quality data in the first instance will help to further maximize the value of attributes.

Acknowledgement

We would like to thank Hong Bing, a researcher in Institute of Geochemistry, Chinese Academy of Sciences for providing their GPR equipment and technical support. This study was supported by the National Key Research and Development Program of China [2016YFC0502602]; the National Nature Science Foundation of China [41571130074, U1612441, 41403112]; the International Partnership Project [132852KYSB20170029], and Guizhou Provincial Science and Technology Department Project [(2018)5405]. We also thank two anonymous referees and the editor for their constructive comments and suggestions that have improved the quality of the paper

References

Al-fares, W., Bakalowicz, M., Guérin, R., Dukhan, M., 2002. Analysis of the karst aquifer structure of the Lamalou area (Hérault, France) with ground penetrating radar. J. Appl. Geophys. 51, 97–106. https://doi.org/10.1016/S0926-9851(02)00215-X

Alsharahi, G., Mostapha, A.M.M., Faize, A., Driouach, A., 2016. Modelling and simulation resolution of ground-penetrating radar antennas. J. Electromagn. Eng. Sci. 16, 182–190. https://doi.org/10.5515/JKIEES.2016.16.3.182

Bahorich, M., Farmer, S., 1995. 3-D Seismic Discontinuity for Faults and Stratigraphic Features: The Coherence Cube. Lead. Edge 14, 1053-1058. https://doi.org/10.1190/1.1437077

Bakalowicz M., 2004: The Epikarst, the Skin of Karst. -Karst Waters Institute Special Publication 9, pp 16-21

Bradford, J.H., Deeds, J.C., 2006. Ground-penetrating radar theory and application of thin-bed offset-dependent reflectivity. Geophysics 71. https://doi.org/10.1190/1.2194524

Čeru, T., Šegina, E., Knez, M., Benac, Č., Gosar, A., 2018. Detecting and characterizing unroofed caves by ground penetrating radar. Geomorphology 303, 524–539. https://doi.org/10.1016/j.geomorph.2017.11.004

Chalikakis, K., Plagnes, V., Guerin, R., Valois, R., Bosch, F.P., 2011. Contribution of geophysical methods to karst-system exploration: An overview. Hydrogeol. J. 19, 1169–1180. https://doi.org/10.1007/s10040-011-0746-x

Chen, Q., Sidney, S., 1997. Seismic attribute technology for reservoir forecasting and monitoring. Lead. Edge 16, 445–448. https://doi.org/10.1190/1.1437657

Chen, X.P., 1997. Research on characteristics of soil erosion in karst mountainous region environment. Journal of Soil Erosion and Soil and Water Conservation, 3, 31–36. http://dx.chinadoi.cn/10.13870/j.cnki.stbcxb.1997.04.006

Chopra, S., Marfurt, K.J., 2005. Seismic attributes - A historical perspective. Geophysics 70, 3SO-28SO. https://doi.org/10.1190/1.2098670

Doolittle, J.A., Collins, M.E., 1998. A comparison of EM induction and GPR methods in areas of karst. Geoderma 85, 83–102. https://doi.org/10.1016/S0016-7061(98)00012-3

Feng, Z.G., Wang, S.J., Liu, X.M., 2009. Impact of acid-insoluble residua of carbonate rocks on developing intensities of their weathering crusts. Acta Geologica Sinica, 83: 885–893. http://dx.doi.org/10.3321/j.issn:0001-5717.2009.06.016

Fisher, E., Mcmechan, G.A., Annan, A.P., 1992. Acquisition and processing of wide-aperture ground-penetrating radar data. Geophysics 57, 495–504. https://doi.org/10.1190/1.1443265

Forte, E., Pipan, M., Casabianca, D., Di Cuia, R., Riva, A., 2012. Imaging and characterization of a carbonate hydrocarbon reservoir analogue using GPR attributes. J. Appl. Geophys. 81, 76–87. https://doi.org/10.1016/j.jappgeo.2011.09.009

Franseen, E.K., Byrnes, A.P., Xia, J., Miller, R.D., 2007. Improving resolution and understanding controls on GPR response in carbonate strata: Implications for attribute analysis. Lead. Edge 26, 984–993. https://doi.org/10.1190/1.2769554

Jiang, Z., Wang, R., Fei, J., 2001. Epikarst zone in south China and its regulation function to karst water. Carsologica Sinica 20: 106–110. (in Chinese)

Jol, H.M., 2009. Ground Penetrating Radar: Theory and Applications. Elsevier Science, Amsterdam. https://doi.org/10.1016/B978-0-444-53348-7.00019-3

Jones, W.K., 2013. Physical Structure of the Epikarst Fizična struktura epikrasa. Acta Carsologica 42, 311–314. https://doi.org/10.3986/ac.v42i2-3.672

Jukić, D., Denić-Jukić, V., 2009. Groundwater balance estimation in karst by using a conceptual rainfall-runoff model. J. Hydrol. 373, 302–315. https://doi.org/10.1016/j.jhydrol.2009.04.035

Julayusefi M., Goudarzi A.R., Bovanloo R.H., Shamounzadeh M., 2012. Application of the 2-D dual-tree CWT as an image processing technique to attenuate remnant random noise of GPR signals. SEG Global Meeting Abstracts : 1-4. https://doi.org/10.1190/IST092012-001.78

Labat, D., Ababou, R., Mangin, A., 1999. Linear and nonlinear input/output models for karstic springflow and flood prediction at different time scales. Stoch. Environ. Res. Risk Assess. 13, 337–364. https://doi.org/10.1007/s004770050055

Lavelle，P., Decaëns，T., Aubert, M., et al, 2006. Soil invertebrates and ecosystem services. Eur. J. Soil Biol. 42, S3 – S15. https://doi.org/10.1016/j.ejsobi.2006.10.002

Liang, X., Zhu, Z., Liang, B., *et al*, 2003.Preliminary analysis on hydro-geochemical characteristics of the epikarst zone in Luota, Hunan. Carsologica Sinica, 22: 103-109. (in Chinese)

Liu, Z., Li, Q., Sun, H., Wang, J., 2007. Seasonal, diurnal and storm-scale hydrochemical variations of typical epikarst springs in subtropical karst areas of SW China: Soil CO2 and dilution effects. J. Hydrol. 337, 207–223. https://doi.org/10.1016/j.jhydrol.2007.01.034

Mangin, A., 1974: Contribution a l' etude hydrodynamique des aquiferes karstiques. Anndles de Speleclogie. 29: 283-332

McNeill, J.D., 1991. Advances in electromagnetic methods for groundwater studies. Geoexploration 27, 65–80. https://doi.org/10.1016/0016-7142(91)90015-5

Mitrofan, H., Povară, I., Mafteiu, M., 2008. Geoelectrical investigations by means of resistivity methods in karst areas in Romania. Environ. Geol. 55, 405–413. https://doi.org/10.1007/s00254-007-0986-1

Neal, A., 2004. Ground-penetrating radar and its use in sedimentology : principles , problems and progress. Earth-Science Rev. 66, 261–330. https://doi.org/10.1016/j.earscirev.2004.01.004

Peng, T., Wang, S., 2012. Effects of land use, land cover and rainfall regimes on the surface runoff and soil loss on karst slopes in southwest China. Catena 90, 53–62. https://doi.org/10.1016/j.catena.2011.11.001

Reis, J.A. dos, de Castro, D.L., de Jesus, T.E.S., Filho, F.P.L., 2014. Characterization of collapsed paleocave systems using GPR attributes. J. Appl. Geophys. 103, 43–56. https://doi.org/10.1016/j.jappgeo.2014.01.007

Steelman, C.M., Kennedy, C.S., Parker, B.L., 2015. Geophysical conceptualization of a fractured sedimentary bedrock riverbed using ground-penetrating radar and induced electrical conductivity. J. Hydrol. 521, 433–446. https://doi.org/10.1016/j.jhydrol.2014.12.001

Theune, U., Sacchi, M.D., Schmitt, D.R., 2006. Least-squares local Radon transforms for dip-dependent GPR image decomposition. J. Appl. Geophys. 59, 224–235. https://doi.org/10.1016/j.jappgeo.2005.10.003

Wang, B., Tian, G., Cui, X., Zhang, X., 2008. The internal COF features in Dome A of Antarctica revealed by multi-polarization-plane RES. Appl. Geophys. 5, 230–237. https://doi.org/10.1007/s11770-008-0029-z

Williams, P. W. 1983: The role of the subcutaneous zone in karst hydrology. -Journal of Hydrology, 61, 45−67. Doi: 10.1016/0022-1694(83)90234-2

Yan, D., Zhang, X., Wen, A., He, X. Bin, Long, Y., 2012. Assessment of sediment yield in a small karst catchment by using 137Cs tracer technique. Int. J. Sediment Res. 27, 547–554. https://doi.org/10.1016/S1001-6279(13)60012-8

Young, R.A., Deng, Z., Sun, J., 1995. Interactive processing of GPR data. Lead. Edge (Tulsa, OK) 14, 275–280. https://doi.org/10.1190/1.1437130

Young, R.A., Deng, Z., Marfurt, K.J., Nissen, S.E., 1997. 3-D dip filtering and coherence applied to GPR data: A study. Lead. Edge 16, 921. https://doi.org/10.1190/1.1437699

Yuan, D., *et al*, 2016: Modern Karstology. Science Press, Beijing.

Zajícová, K., Chuman, T., 2019. Application of ground penetrating radar methods in soil studies : A review. Geoderma 343, 116–129. https://doi.org/10.1016/j.geoderma.2019.02.024

Zeng, Z., Liu, S., et al, 2010. Ground penetrating radar principle and application. Publishing House of Electronics Industry, pp54, Beijing.

Zhang, C., Yuan, D., Cao, J., 2005. Analysis of the environmental sensitivities of a typical dynamic epikarst system at the Nongla monitoring site, Guangxi, China. Environ. Geol. 47, 615–619. https://doi.org/10.1007/s00254-004-1186-x

Zhao, W., Chen, G., Tian, G., Wang, B., 2012. Progress in ground penetrating radar attribute technology. Progress in Geophysics 27: 1262-1267. doi:10.6038/j.issn.1004-2903.2012.03.054

Zhao, W., Forte, E., Pipan, M., Tian, G., 2013. Ground Penetrating Radar (GPR) attribute analysis for archaeological prospection. J. Appl. Geophys. 97, 107–117. https://doi.org/10.1016/j.jappgeo.2013.04.010